March 2003

Imaging Live Cells Under Mechanical Stress

Brian P. Helmke
University of Virginia

Peter F. Davies
University of Pennsylvania, pfd@pobox.upenn.edu

Reprinted from *Live Cell Imaging: A Laboratory Manual*, edited by Robert D. Goldman and David Spector (Cold Spring Harbor, New York: Cold Spring Harbor Laboratory Press, 2005), chapter 33.

Imaging Live Cells Under Mechanical Stress

Abstract
Cellular responses to mechanical stimuli are implicated in the structural and functional adaptation of many tissues. For example, cellular mechanisms mediate bone and skeletal muscle remodeling during mechanical loading, lung function during ventilator-induced injury, hearing loss in the inner ear, and blood flow-mediated cardiovascular pathophysiology. Since much of our own work investigates vascular biomechanics, we will focus in this chapter on the techniques used to study vascular endothelial cells in vitro; however, similar techniques can be used to study other cell types.

Comments
Reprinted from *Live Cell Imaging: A Laboratory Manual*, edited by Robert D. Goldman and David Spector (Cold Spring Harbor, New York: Cold Spring Harbor Laboratory Press, 2005), chapter 33.

In: "Imaging Live Cells: A Laboratory Manual" Ed. Spector, D.L., Goldman, R.L. Cold Spring Harbor Laboratory Press In Press March 2003

IMAGING LIVE CELLS UNDER MECHANICAL STRESS

Brian P. Helmke[1] and Peter F. Davies[2]

[1]Department of Biomedical Engineering and Cardiovascular Research Center, University of Virginia

and

[2]Department of Pathology and Laboratory Medicine and Institute for Medicine and Engineering, University of Pennsylvania

Address for correspondence:

Brian P. Helmke, Ph.D.
Univ. of Virginia
Dept. of Biomedical Engineering
P. O. Box 800759
Charlottesville, VA 22908
Tel: 434-924-1726
Fax: 434-982-3870
Email: helmke@virginia.edu

Peter F. Davies, Ph.D.
Univ. of Pennsylvania
Inst. for Medicine and Engineering
1010 Vagelos Research Labs
3340 Smith Walk
Philadelphia, PA 19104
Tel: 215-573-6813
Fax: 215-573-6815
Email: pfd@pobox.upenn.edu

INTRODUCTION

Cellular responses to mechanical stimuli are implicated in the structural and functional adaptation of many tissues. For example, cellular mechanisms mediate bone and skeletal muscle remodeling during mechanical loading, lung function during ventilator-induced injury, hearing loss in the inner ear, and blood flow-mediated cardiovascular pathophysiology. Since much of our own work investigates vascular biomechanics, we will focus in this chapter on the techniques used to study vascular endothelial cells in vitro; however, similar techniques can be used to study other cell types.

Why Image Vascular Cells Under Mechanical Stress In Vitro?

In the blood vessel wall, two primary mechanisms for arteriolar autoregulation of blood flow depend on vascular wall cell functions. First, flow-mediated vasodilation occurs in response to increased frictional shear stress acting on the endothelium at the blood-tissue interface. Mechanochemical signals from endothelial cells cause adjacent smooth cells to relax, thereby increasing vessel diameter. This reduces the pressure gradient driving flow through the vessel and returns volumetric flow rate back to baseline. Second, an increase in arteriolar pressure or the circumferential stretch of the vessel wall induces vascular smooth muscle cell contraction that results in vasoconstriction. This myogenic response limits volumetric flow through the vessel and returns the flow rate to baseline levels. Physiological control of blood flow to peripheral organs depends on a balance of these two acute vasoregulatory responses.

Although intravital microscopy allows access to cellular behavior in the microcirculation **(see Whole Imaging of the Vascular System in Mouse by Rakesh Jain)**, direct measurements of intercellular interactions or intracellular dynamics in response to mechanical stimuli in larger

arteries are challenging. In addition, precise measurement of the local hemodynamic force profile is often technically difficult, and physiological variation among subjects prevents control of fluid dynamics parameters. Furthermore, the complexity of the in vivo environment often prevents accurate elucidation of mechanisms. In vitro models of mechanical stimulation provide a means to precisely control the stimulus and monitor cellular responses. From a biomedical engineering perspective, this allows development of predictive models of cell behavior that will lead to new therapeutic approaches based on control of vascular function.

In vitro models for applying shear stress to endothelial cells rely on flow chambers that only recently have been optimized for visualization of living cells. Image acquisition methods with such chambers obtain the higher temporal and spatial resolution necessary for understanding cell-mediated mechanisms that direct vascular function. For example, hemodynamic shear stress rapidly induces transient intracellular events that play a role in the activation of multiple signaling networks (Davies, 1995). The fastest of these events include heterotrimeric G protein activation, opening of chloride, potassium, and volume-regulated anion channels, increased intracellular calcium concentration, and production of chemical mediators such as nitric oxide and prostaglandins. These events occur within seconds after a change in the local hemodynamic profile, requiring rapid measurement of biochemical functions during application of fluid shear stress. Although temporal changes of cellular responses can often be measured indirectly, detection of the spatial distribution of mechanical and chemical responses within the cell requires direct visualization. Examples include preferential locations of increased membrane lipid lateral mobility and heterogeneous displacement, deformation, and polymerization of cytoskeletal elements. Such events must be monitored on a subcellular length scale in order to elucidate mechanisms of mechanochemical sensing. Thus, live-cell imaging

during extracellular force application is required in order to capture mechanically induced responses with enough detail to investigate mechanochemical signaling mechanisms.

Relating Live Cell Imaging to Biomechanical Models

Phenomenological models have been derived based on generalized cell structures in an attempt to explain cell behavior in response to applied forces, and the mechanical properties of the cytoplasm have been proposed to depend on the cytoskeletal architecture. In one model, a tensegrity structure represents the cytoskeleton as an interconnected network of tension-bearing elastic filaments and compression-bearing struts that exists in a state of prestress (Wang et al., 1993). Indeed, experimental disruption of adhesion sites near the cell edge results in apparent elastic recoil towards the cell body. This model has been extended to the nucleus after experimental demonstration of nuclear deformation in response to pulling on the cell surface. An alternative model suggests that the cytoplasmic cytoskeleton is a viscoelastic polymer gel that undergoes phase transitions in response to applied stress or strain. In this model, locally applied forces are dissipated with distance away from the site of force application so that the applied force is not directly sensed at remote locations within the cell (Heidemann et al., 1999). Relatively local displacement of cytoskeleton-associated elements during poking with a micropipette or twisting of magnetic beads on the cell surface supports this model. It is clear that mechanical responses within the cytoplasm that mediate mechanochemical signal transduction are integrated in a complex manner that is not well understood. High-resolution live cell imaging of cells under mechanical stress provides experimental access to test these models.

Recent advances in image analysis of live-cell images are revealing new details relevant to mechanical interactions predicted by these models at a subcellular length scale. For example, onset of shear stress induces heterogeneous displacement of intermediate filaments, implying

that fluid shear stress induces spatial gradients of mechanical events in the cytoskeleton. Mechanical strain computed in the intermediate filament network is highly focused at discrete locations within the cell, suggesting that cytoskeletal tension is redistributed to sites that are putatively associated with signaling molecule scaffolds such as focal adhesion sites. Such strain focusing was only detectable after careful quantitative analysis of 4-D fluorescence data in living endothelial cells during onset of shear stress **(see below)**. These quantitative optical analyses have revealed new details of intracellular mechanical behavior that is relevant to the initiation of mechanochemical signal transduction.

CHAMBERS FOR OBSERVING LIVE CELLS UNDER MECHANICAL STRESS

Many of the considerations discussed in previous chapters **(see Setting Up to Image Live Mammalian Cells by Jason Swedlow)** are critical for the successful imaging of live cell processes under mechanical stress. These include temperature control of both the chamber and the objective lens and maintenance of sterility for long-term observation of cellular adaptation to mechanical force. In addition, for accurate 3-D fluorescence reconstruction of intracellular processes, a No. 1.5 coverslip must be used, since the design of most microscope objectives is optimized for glass coverslips that are 170 μm <micrometers> thick. The fluid medium should be chosen to minimize its contribution to measured fluorescence intensity, as described in **Setting Up to Image Live Mammalian Cells by Jason Swedlow** and **Imaging the Dynamics of Cellular Organelles by multiple authors**. Special consideration is given here to imaging live cells during force application.

Coverslip Stability during Force Application

For accurate time-lapse imaging at subcellular resolution, several sources of error associated with coverslip movement must be minimized or eliminated. Air currents or temperature changes near the microscope stage often cause focus drift. To minimize room air currents, choose a location for the microscope that has relatively constant airflow and temperature, or deflect airflow from vents away from the microscope. For closed chamber experiments, it may be possible to locally block airflow around the chamber by isolating the microscope stage within an environmental chamber. This also reduces temperature variation during overnight experiments in locations where energy conservation requires adjusting thermostat settings during night hours. Fluid introduced into the observation chamber should be at the same temperature as that already in the chamber to prevent focus drift due to temperature gradients associated with convection. Furthermore, high numerical aperture objective lenses should be warmed to minimize heat loss through the immersion fluid.

Experimental interventions required to apply mechanical forces on cells may induce 3-D coverslip displacement. Chamber designs using thicker glass reduce the amount of coverslip displacement during force application, but the No. 1.5 coverslip required for high-resolution fluorescence imaging often flexes significantly with force application on the cells. Displacement of cellular components is subtracted from coverslip movement by including stationary fiducial markers on the coverslip during the time-lapse experiment. For example, fluorescent microspheres on the coverslip underneath the cells are tracked to measure coverslip displacement **(see method below)**. Microspheres with diameter 100 nm or less are easily detectable using high numerical aperture optics, and a fluorescence wavelength is chosen that does not interfere with experimental measurements. In 3-D images, a coplanar set of microspheres indicates the plane of

the coverslip surface. In 2-D images, a set of microspheres should be chosen that maintains constant geometry among points and is continuously in focus to maximize the probability that the microspheres are on the coverslip surface. The displacement of such a set of microspheres represents coverslip displacement during the experiment, and subtracting the change in microsphere positions as a function of time yields true cellular motions.

The following procedure yields a surface density of approx. 3 x 10^5 microspheres/cm^2 using 100-nm microspheres. This density typically gives a coplanar set of approx. 3 microspheres/cell in a confluent monolayer.

Coating Coverslips with Microspheres

1. Sonicate a suspension (2% solids) of 100-nm fluorescent carboxylate-modified polystyrene microspheres for approx. 5 minutes to achieve a monodisperse suspension. A 2% suspension of 0.1-μm <micrometer> diameter polystyrene microspheres has a concentration of 3.6 x 10^{11} microspheres/ml. This is computed from the following equation: $\frac{\text{microspheres}}{\text{ml}} = \frac{6C \times 10^{12}}{\pi \rho \phi^3}$, where C = concentration of microspheres in g/ml (e.g., 0.02 g/ml for a 2% solids suspension), ρ <rho> = polymer density in g/ml (1.05 for polystyrene), and ϕ <phi> = microsphere diameter in μm <micrometers>.
2. Suspension A: Make a 1:1000 dilution of the microsphere suspension in 100% ethanol. E.g., add 1 μl <microliter> microsphere suspension to 999 μl <microliter> ethanol. Note: it is important to use pure ethanol as the solvent since water will leave a residue on the coverslip after evaporation that will scatter light during fluorescence imaging.
3. Suspension B: Make a 1:100 dilution of Suspension A in 100% ethanol. E.g., add 1 μl <microliter> Suspension A to 99 μl <microliter> ethanol. The total dilution factor of Steps 2 and 3 is 10^5, yielding a final concentration of 3.6 x 10^6 microspheres/ml.

4. Compute the surface area (in cm^2) of the coverslip to be coated with microspheres.
5. Compute the required volume of Suspension B (in ml) from (0.08) x (surface area in cm^2). For example, a 4-cm diameter circular coverslip has a surface area of 12.6 cm^2 and requires approx. 1.0 ml of Suspension B.
6. Place a sterile dry coverslip into the center of a tissue culture dish in a laminar flow hood. Do not let the coverslip touch the edges of the dish. Carefully pipette the required volume of Suspension B onto the coverslip, creating a surface tension bubble. Allow the coverslip to dry completely by evaporation.
7. Follow usual procedures for plating cells onto dry, microsphere-coated coverslips.

Timing of Transient Transfection using GFP Fusion Proteins

For experiments imaging live cells under mechanical stress, GFP fusion proteins are often used to visualize structural proteins. In the case of endothelial cells, a confluent monolayer is desired to represent a physiological model. Transient transfection using liposomes induces only about 10–15% of endothelial cells to express GFP so that details of structural dynamics within a single cell in the monolayer can be measured. The timing of an experiment should be planned to simultaneously optimize expression levels of GFP fusion proteins and cell density. Maximum expression of EGFP (Enhanced GFP) typically occurs at approx. 48 hours after transfection, but timing of expression varies slightly with the choice of GFP variant. However, since liposome-mediated transfection is performed at low cell density, confluence may not be achieved until at least 3-4 days after transfection, depending on the population doubling rate. The following procedure yields a compromise between GFP expression and obtaining a confluent monolayer on 4-cm diameter circular coverslips. The timing and cell numbers should be adjusted as necessary for varying expression levels, coverslip surface areas, and cell proliferation rates.

Transfection and Plating Procedure for 4-cm Coverslips

1. Plate endothelial cells in a 6-cm dish at a density of 2.5 x 10^4 cells/cm^2. Allow cells to spread for approx. 16 hours in complete growth medium.
2. Transfect the endothelial cells with 3-11 μg <microgram> DNA plasmid per dish in low serum medium (e.g., OptiMEM I, Gibco) using a liposomal method (e.g., Lipofectin, Gibco). The amount of DNA required varies slightly with the plasmid used and should be optimized in dose response studies.
3. Allow the cells to recover overnight in complete growth medium.
4. Replate the cells onto 4-cm diameter sterile glass coverslips that have been pre-coated with fluorescent microspheres (**see method above**). The cell density should be at least 7 x 10^4 cells/cm^2.
5. **Optional**: If the cell density is too low, non-transfected endothelial cells from the same line can be added into the suspension before plating to achieve the desired density. This will reduce the proportion of cells expressing GFP but will aid in achieving a confluent monolayer.
6. Allow the cells to grow to a confluent monolayer, usually about 2 days after plating.

Open Chambers for Access to the Cell Surface

Manual measurement and manipulation of the cell surface requires access to the cells, usually in an open chamber. As discussed above and in **Setting Up to Image Live Mammalian Cells by Jason Swedlow**, temperature-controlled chambers or stage inserts are preferred for maintaining physiological activity during the experiment. For example, heated culture dishes with coverslip glass bottoms (Bioptechs) permit high-resolution fluorescence microscopy of living cells during force application. In addition, an objective lens heater should be used with high numerical aperture lenses to minimize heat loss through the immersion fluid.

For open chambers it is also important to maintain pH during experiments. One method is to use a basal medium containing an organic buffer such as HEPES instead of bicarbonate, since standard bicarbonate buffers will become basic when equilibrated with atmospheric levels of carbon dioxide. Alternatively, the microscope stage may be enclosed in an incubation chamber equilibrated with 5% CO_2-95% air to mimic incubator conditions. This second approach has the advantage that temperature can be controlled simultaneously by heating the gas flowing into the stage chamber. However, physical access to the cell chamber is often limited, and that may be a disadvantage when using larger instruments or if frequent intervention is needed.

Two examples of force application using open chambers are discussed below.

Deforming the Endothelial Surface using Microneedles

An example of an open chamber application is deforming the cell surface with a glass microneedle. Microneedles are pulled from borosilicate glass capillary tubes using a micropipette puller. A tip diameter of approx. 1 μm <micrometer> allows application of force locally on the cell surface. Force can be applied nonspecifically to the surface, or specific adhesion receptors can be engaged by coating the microneedle with extracellular matrix ligands such as fibronectin, laminin, or collagen. The stiffness, or bending modulus, of the microneedle can be calibrated to compute the applied force from the amount of microneedle deflection while pushing on the cell surface. In one method for calibration, thin wires with known mass are hung from the microneedle, and the needle deflection distance at the tip is measured optically. A typical range of stiffness is of order of magnitude 10-30 nN/μm <nanonewtons/micrometer> (Davidson et al., 1999). By this method known forces are applied to the cell surface.

Flow Chambers for Application of Shear Stress

Cell-mediated responses to fluid flows have recently generated interest in mechanobiology. Application of well-defined flow forces onto the cell surface is necessary to elucidate mechanisms of mechanochemical signaling in endothelium and other cell types. In addition, selection of chambers compatible with high-resolution fluorescence microscopy permits dynamic measurements in living cells during changes in extracellular fluid forces.

Fluid Dynamics Considerations

For most cell culture experiments, cells are exposed to flow of an incompressible Newtonian fluid which is typically complete growth medium or physiological buffer. Incompressibility implies that the fluid has constant density, independent of flow rate. For a Newtonian fluid the shear stress is linearly proportional to the shear rate, and the constant of proportionality is the viscosity. The motion of this fluid is predicted from the basic conservation equations of mass and momentum. These equations of motion are called the Navier-Stokes equations:

$$\rho \frac{D\vec{v}}{Dt} = \rho \frac{\partial \vec{v}}{\partial t} + \rho \vec{v} \cdot \nabla \vec{v} = -\nabla p + \mu \nabla^2 \vec{v} \qquad (1)$$

where $<\vec{v}>$ is the velocity vector of a local fluid "particle", p is the hydrodynamic pressure, ρ <rho> is the fluid density, μ <mu> is the fluid kinematic viscosity, D/Dt is the material derivative, $<\nabla>$ is the gradient operator, and $<\nabla^2>$ is the Laplace operator. It is beyond the scope of this chapter to derive and solve these equations; however, well-characterized special cases will be discussed below.

Variations in biological response have been reported based on whether the flow profile is laminar or turbulent. In the laminar flow regime, the fluid can be described qualitatively as

"sheets" or layers of fluid sliding past each other with continuous variation in speed from one layer to the next. In contrast, turbulent flow is characterized by random fluctuations in velocity of individual fluid "particles" superimposed on the mean bulk fluid motion. The tendency towards turbulence is determined by the ratio of magnitudes of inertial forces to viscous damping forces described by a dimensionless parameter called the Reynolds number:

$$\mathrm{Re} = \frac{\rho v L}{\mu} = \frac{v L}{\nu} \tag{2}$$

where v <letter vee> is the mean fluid velocity, ν <nu> is the kinematic viscosity of the fluid, and L is a characteristic length associated with the flow. By convention, the characteristic length for a parallel plate flow chamber is its height, and L for a glass tube is its diameter. A higher Reynolds number indicates a higher probability of turbulent fluid structure as viscous damping becomes dominated by fluid inertia. The transition typically occurs for Reynolds numbers in the range 1400-2300, depending on geometry. Most physiological flows fall in the laminar regime. However, a few examples of turbulent flows exist, such as airflow during cough or sneeze, blood flow in the aortic arch during peak systole, and blood flow in the brachial artery during blood pressure measurement with a sphygmomanometer. In addition, turbulent flows often diagnose pathological states of blood flow, including heart valve insufficiency (heart murmur) or arterial stenosis.

The design of an experimental setup depends on the flow chamber geometry and desired flow profile. Perfusion with a syringe pump is acceptable for short experiments with low volume flow rates. However, this may not be adequate for long-term experiments to study cell adaptation or for more complicated flow profiles. In this case a continuous closed flow loop is used (**Figure 1**). A closed loop assembled aseptically in a biosafety cabinet prevents contamination during experimental observation on the microscope, and the perfusion method can be designed to

produce the desired flow profile. For steady flow, a constant volume flow rate is driven by gravity from an upstream reservoir positioned above the microscope stage. The hydrostatic driving pressure varies linearly with the height of the reservoir. Fluid is drained out of the chamber into a downstream reservoir, and a peristaltic pump recirculates the fluid back into the upstream reservoir. Bicarbonate-containing culture medium is maintained at proper pH by equilibrating it with humidified gas containing 5% CO_2-95% air, and the downstream reservoir is heated to maintain temperature.

Parallel Plate Flow Chambers

Parallel plate flow chambers are widely used in experimental studies of fluid dynamics effects on cultured cells. If the height-to-width and height-to-length ratios of the chamber dimensions are small (typically <1/50), then a fully developed parabolic velocity profile is sufficient to compute the shear stress acting on the cells. In this case, the only non-zero component of velocity is in the direction of flow and is a function of height in the chamber:

$$v(y) = \frac{3Q}{2wh}\left[1 - \left(\frac{2y}{h}\right)^2\right] \tag{3}$$

where v <letter vee> is velocity, Q is volume flow rate, w and h are the width and length of the chamber, and y is the vertical distance from the centerline between the two parallel plates. From this equation the shear stress τ <tau> is derived from the product of the velocity gradient and fluid viscosity μ <mu> as

$$\tau(y) = -\mu\frac{dv}{dy} = \frac{12\mu Q}{wh^3}y \tag{4}$$

For a fluid with constant viscosity, equation 4 shows that the shear stress is zero at the centerline between the parallel plates and increases linearly to a maximum on the plate surface, where the wall shear stress is given by

$$\tau_w = \frac{6\mu Q}{wh^2} \tag{5}$$

For imaging live cell under stress, two parallel plate flow chamber designs are commonly used. In the first (Frangos et al., 1988), cells are grown on a coverslip that is assembled onto the bottom of the flow chamber and held in place by a vacuum seal around the edge. This design is easy to assemble and disassemble quickly so that shear stress can be applied for only seconds, and cells can be recovered rapidly for biochemical assays such as protein phosphorylation or G protein activation. In this design, temperature is maintained by perfusion of warmed fluid. A second design by Bioptechs (model FCS2, Butler, PA) is more convenient for reducing the shear stress to zero, since the coverslip and top plate of the chamber are maintained at the desired temperature (usually 37 ºC). In addition, the top plate in the Bioptechs chamber is optically clear to allow high-resolution transillumination microscopy in brightfield, phase contrast, or differential interference contrast (DIC) modes. In both of these chamber designs, the Reynolds number typically lies in the range 0-20 so that a fully developed parabolic velocity profile exists everywhere in the chamber except at the entrance; the entrance length necessary to achieve a fully developed velocity profile is approximately 1/100 of the chamber length.

Parallel Plate Flow Chamber with Physical Access to the Cells

In order to directly access cells for measurement and manipulation during exposure to hemodynamics forces, we have designed a parallel plate flow chamber that permits instrument access to adherent cells with minimal disturbance of the velocity field (Levitan et al., 2000).

Based on the parallel plate flow chamber design, the "minimally invasive flow device" (MIF device) has 1-mm wide longitudinal slits cut into the top plate of the chamber to allow insertion of a recording, measurement, or stimulating instrument. Surface tension forces at the slit openings are larger than the hydrodynamic pressure in the chamber, so overflow through the slits is prevented over a physiological range of steady shear stress (0 to 15 dyn/cm^2). The components and assembled chamber are shown in **Figure 2**. A probe such as a micropipette is positioned near the cell surface, makes direct contact with the cell membrane, or enters the cell while inducing negligible deviations in laminar flow near the cell surface, as demonstrated by monitoring the trajectories of microspheres in the fluid. For example, the MIF device has enabled measurement of flow-induced changes in membrane potential using patch clamp electrophysiological techniques. The MIF device offers numerous possibilities to investigate real-time endothelial responses to well-defined flow conditions in vitro using electrophysiology and amperometric techniques, cell surface mechanical probing, local controlled chemical release or biosensing, and microinjection (**Figure 3**).

Glass Capillary Tubes

Endothelial cells have been cultured in glass capillary tubes with either circular or rectangular cross-section. Cylindrical tubes have the advantage of more closely modeling the in vivo geometry of blood vessels, especially if small tubes are chosen to match blood vessel diameter and radius of curvature. Rectilinear tubes provide a close approximation to vessel geometry with the additional advantage that cells are grown on an optically flat surface that allows high-resolution microscopy. Disadvantages include limited numbers of cells, which often prevents biochemical assays subsequent to imaging measurements.

For Reynolds numbers in the laminar flow regime, the Navier-Stokes equations can be solved for the velocity profile as a 1-D function of radius:

$$v(r) = \frac{2Q}{\pi a^2}\left[1 - \left(\frac{r}{a}\right)^2\right] \tag{6}$$

where a is the tube radius and r is radial distance from the centerline of the tube. For a Newtonian fluid with constant viscosity the shear stress is given by

$$\tau(r) = -\mu\frac{dv}{dr} = \frac{4\mu Q}{\pi a^4}r \tag{7}$$

and the shear stress at the wall is

$$\tau_w = \frac{4\mu Q}{\pi a^3} \tag{8}$$

The precision of manufacturing glass capillary tubes is important to accurately compute the shear stress profile. Reliable sources include Stoelting (Kiel, WI) and VitroCom (Mountain Lakes, NJ). Tubes with wall thickness of 0.17 mm, optimal for high-resolution microscopy, are available from VitroCom. A tight connection into the flow loop can be made directly from tubing with internal diameter slightly smaller than the outer diameter of the glass tube. For rectilinear tubes, connections can be sealed by carefully wrapping the end of the glass tube with Parafilm™ before connecting the flow loop tubing. To maintain sterility, Parafilm™ must not touch the fluid inside the glass tube.

ENGINEERING ANALYSIS OF RAPID INTRACELLULAR EVENTS INDUCED BY MECHANICAL STRESS

Analysis of Intermediate Filament Displacement

Using the methods discussed above, confluent monolayers of endothelial cells expressing GFP-vimentin were observed in the Bioptechs parallel plate flow chamber. Stacks of optical sections were acquired at 90-second intervals and were deconvolved a constrained iterative algorithm (Agard and Sedat, 1983). GFP-vimentin distributed to the endogenous intermediate filament cytoskeleton (Helmke et al., 2000), which consisted of a prominent perinuclear ring and a mesh network of intermediate filaments radiating toward the cell periphery (**Figure 4 A**). In 3-D images, intermediate filaments were often visible reaching above and below the nucleus. In time-lapse movies, connections among individual filament segments within the intermediate filament network did not appear to change as filaments throughout the cytoplasm fluctuated or "wiggled" in apparently random directions (**Figure 4 B-C**).

Onset of unidirectional laminar shear stress (τ_w <tau[sub]w> = 12 dyn/cm^2) induced significant directional displacement of intermediate filaments in regions of cells. Some filament segments were displaced by almost 1 μm <micrometer> within 3 minutes (**Figure 4 B, D**), although displacement was heterogeneous throughout the cytoplasm in 3-D. Displacement continued with exposure to shear stress, and the rate of displacement varied with position in the cell.

A quantitative method for analyzing the structural dynamics in the cytoskeleton has been developed. The displacement of GFP-vimentin–labeled intermediate filaments is detected by analyzing the fluorescence distribution as a function of spatial location. For example, displacement projected onto the x-axis can be detected by comparing the line intensity profiles

from two time points. Displacement of intensity peaks indicates filament movement in the *x*-direction during the interval, whereas overlapping intensity peaks indicate zero displacement. Changes in peak intensity during the interval indicate displacement into or out of the focal plane.

Quantitative measurement of intermediate filament displacement has been extended to 3-D by analyzing the 4-D fluorescence distribution function $f(x,y,z,t)$ from spatial regions in the image. Analysis of the entire image as a single spatial region yields a measure of degree of displacement throughout the cell but is of limited use due to the constitutive movement of intermediate filaments throughout the cytoplasm. However, analysis of displacement at a subcellular length scale reveals regional heterogeneity of intermediate filament motion. An appropriate length scale is established by analyzing the spatial power spectrum from a 3-D image stack at the beginning of the experiment. In analysis of GFP-vimentin images, subimages were chosen that had dimensions 1.7 μm × 1.7 μm × 0.68 μm <micrometers>. After dividing 3-D images into subimages, the displacement index (DI) is computed from the product moment cross-correlation coefficient, which measures the degree of overlap between fluorescence intensity distributions at two time points. Increasing values of DI indicate increased displacement of intermediate filament segments within the subimage during an interval (Helmke et al., 2001).

Choosing a Length Scale for Subcellular Analysis

1. Read a series of TIFF images into a 3-D matrix f_{xyz} in math software such as Matlab or IDL.
2. Compute the 3-D Fourier transform of the matrix with dimensions X×Y×Z from

$$F_{uvw} = \sum_{x=0}^{X-1}\sum_{y=0}^{Y-1}\sum_{z=0}^{Z-1} f_{xyz} e^{-2\pi i\left(\frac{ux}{X}+\frac{vy}{Y}+\frac{wz}{Z}\right)} \quad (9)$$

where $i = (-1)^{1/2}$. Note that (u,v,w) is the frequency domain coordinate position corresponding to the image coordinate (x,y,z).

3. Compute the power spectrum magnitude matrix from

$$S_{uvw} = F_{uvw} F^*_{uvw} \tag{10}$$

where F^* is the complex conjugate of F obtained by replacing i with $-i$ in Equation 9.

4. Transform the matrix S_{uvw} to cylindrical coordinates $S_{r\theta w}$ where $r^2 = u^2 + v^2$ and $\tan \theta = v/u$.

5. Integrate the matrix S over all θ <theta> and w to yield the projection of the spectrum on the r-axis:

$$S_r = \sum_{w=0}^{W-1} \sum_{\theta=0}^{2\pi} S_{r\theta w} \tag{11}$$

6. Plot S_r vs. r and look for local peaks; these indicate dominant spatial frequencies in the optical plane. The spatial separation corresponding to these frequencies is given by $1/r$. Spatial regions for analysis of displacement should be at least twice this size so that all regions contain at least one filament segment.

7. Determine the minimum region size along the optical axis in a similar manner. Integrate S over all r and θ <theta> to yield the projection on the z-axis:

$$S_w = \sum_{r=0}^{R-1} \sum_{\theta=0}^{2\pi} S_{r\theta w} \tag{12}$$

Note that R is the dimension of the matrix on the r-axis, computed from $R^2 = U^2 + V^2$. Plot S_w vs. w and look for local peaks, indicating dominant spatial frequencies along the optical axis. The spatial separation corresponding to these frequencies is given by $1/w$. Choose spatial regions with a z-dimension of at least twice this size.

Computation of Displacement Index

1. The degree of overlap between fluorescence distributions is inversely correlated to the magnitude of filament displacement within a spatial region. Measure the degree of overlap between images at times *t* and *T* by computing a spatial cross-product moment, or spatial covariance:

$$\mathrm{Cov}\left[f_{xyzt}, f_{xyzT}\right] = \frac{1}{XYZ}\sum_{z=0}^{Z-1}\sum_{y=0}^{Y-1}\sum_{x=0}^{X-1}\left[\left(f_{xyzt} - \hat{f}_{xyzt}\right)\left(f_{xyzT} - \hat{f}_{xyzT}\right)\right] \tag{13}$$

where

$$\hat{f}_{xyzt} = \frac{1}{XYZ}\sum_{z=0}^{Z-1}\sum_{y=0}^{Y-1}\sum_{x=0}^{X-1} f_{xyzt} \tag{14}$$

is the mean intensity in the subregion at time *t*.

2. Compute the spatial variance at each time *t* from

$$\mathrm{Var}\left[f_{xyzt}\right] = \frac{1}{XYZ}\sum_{z=0}^{Z-1}\sum_{y=0}^{Y-1}\sum_{x=0}^{X-1}\left(f_{xyzt} - \hat{f}_{xyzt}\right)^2 \tag{15}$$

3. In order to eliminate the dependence of spatial covariance on the number of non-zero data points and the absolute intensity scale, compute the product moment correlation coefficient using Equations 13 and 15:

$$\mathrm{PMCC}(t,T) = \frac{\mathrm{Cov}\left[f_{xyzt}, f_{xyzT}\right]}{\sqrt{\mathrm{Var}\left[f_{xyzt}\right]\mathrm{Var}\left[f_{xyzT}\right]}} \tag{16}$$

Equation 16 is a measure of the degree of overlap of fluorescence intensity from time *t* to *T* in a spatial region.

4. To simplify interpretation, compute the displacement index as

$$\mathrm{DI}(t,T) = 1 - \mathrm{PMCC}(t,T) \tag{17}$$

The DI has minimum value zero, indicating no displacement, and increases with increasing filament displacement within a spatial region during the time interval.

Analysis of Cytoplasmic Strain from Endogenous Intermediate Filament Networks

The relative displacement of adjacent intermediate filaments indicates mechanical strain in the cytoskeletal network. Since the shear stress acting at the cell surface may be transmitted throughout the cytoplasm via the cytoskeleton, analysis of intracellular strain using endogenous structures will reveal mechanisms that directly relate extracellular mechanical stimuli to initiation of biochemical signaling at discrete locations within the cell.

Computation of Cytoplasmic Strain Field in 2-D Optical Sections

1. Select a time sequence of 2-D optical sections normalized to a constant height above the coverslip. Apply a median filter to minimize high frequency shot noise, and enhance contrast applying a high-pass filter. Apply a low-pass filter to smooth the resulting intensity distribution.
2. In order to optimize the extraction of filament positions, all pixels with intensity below a threshold are set to value zero. Determine a threshold intensity value I_{thresh} from

$$I_{thresh} = \hat{I} - \frac{\sigma}{3} \tag{18}$$

where $<\hat{I}>$ is the global mean intensity and σ <sigma> is the standard deviation of intensity in the optical section. Note that other methods for optimizing the threshold intensity are possible, and the choice depends to some extent on the signal-to-noise ratio in the image.

3. After setting background pixels to zero intensity, create a binary skeleton image (**Figure 5 A**) using built-in functions available in most image processing or math software (e.g., Scion Image, Matlab, IDL).
4. In each skeleton, vertices are defined as positions where three or more filament segments intersect. In the binary skeleton image (black pixels on a white background), identify coordinates of black pixels surrounded by at least three other black pixels. In areas of

dense filament connections, this search may produce clusters of pixels rather than a single pixel coordinate. In this case, the position of the intersection is estimated from the geometric mean of the cluster.

5. Track the vertices from the current time point to the next to obtain the initial (*X*,*Y*,*Z*) and final (*x*,*y*,*z*) coordinates (**Figure 5 B**). Several automated tracking algorithms are readily available. For example, we have implemented a particle tracking algorithm based on a probability model for distance moved between time points (Crocker and Grier, 1996).
6. In order to interpolate the strain field, connect adjacent vertices into triangles using a Delaunay triangulation function (**Figure 5 C**). This function, available in Matlab, creates a set of triangles for which no vertex is located inside another triangle, thereby providing maximum spatial resolution for estimating the strain field.
7. Compute the Lagrangian strain tensor from the shape change of each triangle derived from the initial and final coordinates of the vertices at the corner of the triangle. For each pair of vertices, the Lagrangian strain tensor E_{ij} is a 2×2 matrix computed from

$$ds^2 - ds_0^2 = 2E_{11}dX^2 + 4E_{12}dX \cdot dY + 2E_{22}dY^2 \quad (19)$$

In Equation 19, *dX* is the initial difference between *x*-coordinates and *dY* is the initial difference between *y*-coordinates of the two vertices, ds_0 is the initial distance between the vertices, and *ds* is the final distance between the vertices after deformation. Note that these distances are computed from

$$ds_0^2 = dX^2 + dY^2 \text{ and } ds^2 = dx^2 + dy^2 \quad (20)$$

In Equation 20, *dx* is the difference between final *x*-coordinates and *dy* is the difference between final *y*-coordinates of the two vertices after deformation.

8. Since Equation 19 contains three unknown components of the strain tensor *E*ij, a unique solution is obtained by solving a simultaneous system of three equations derived from the vertex pairs determined by the three sides of each triangle. The resulting strain tensor

describes the average deformation for the spatial region. The strain magnitude can then be mapped to the skeleton in the optical section (**Figure 5 D**).

9. The eigenvalues of E_{ij} are the principal values of strain oriented along the principal axes determined by the unit eigenvectors of the matrix. The principal values are the maximum and minimum values of strain in the spatial region for an equivalent strain field that contains zero shear components. For methods of computing the eigenvectors of a matrix the reader is referred to linear algebra texts, e.g. (Boas, 1983).
10. In some cases it is desirable to express the principal values of strain E_1 and E_2 as stretch ratios λ_1 <lambda> and λ_2, computed from

$$E_i = \frac{1}{2}\left(\lambda_i^2 - 1\right) \tag{21}$$

where the subscript i has values 1 and 2 corresponding to the principal axes. In particular, note that if the product of principal stretch ratios $\lambda_1\lambda_2$ <lambda> is unity, then area of the triangle is conserved during deformation.

ACKNOWLEDGEMENTS

We gratefully acknowledge the assistance of David Thakker and Amy Rosen during the development of these techniques and valued discussions with Drs. John Murray, Paul Janmey, and Arjun Yodh of the University of Pennsylvania. Dr. Robert Goldman graciously provided a GFP-vimentin DNA construct that enabled the initial studies of intermediate filament dynamics.

REFERENCES

Agard, D. A. and Sedat, J. W. (1983). Three-dimensional architecture of a polytene nucleus. *Nature* **302**, 676-81.

Boas, M. L. (1983). Mathematical Methods in the Physical Sciences. New York: John Wiley & Sons.

Crocker, J. C. and Grier, D. G. (1996). Methods of digital video microscopy for colloidal studies. *Journal of Colloid and Interface Science* **179**, 298-310.

Davidson, L. A., Oster, G. F., Keller, R. E. and Koehl, M. A. R. (1999). Measurements of mechanical properties of the blastula wall reveal which hypothesized mechanisms of primary invagination are physically plausible in the sea urchin *Strongylocentrotus purpuratus*. *Developmental Biology* **209**, 221-238.

Davies, P. F. (1995). Flow-mediated endothelial mechanotransduction. *Physiological Reviews* **75**, 519-560.

Frangos, J. A., McIntire, L. V. and Eskin, S. G. (1988). Shear stress induced stimulation of mammalian cell metabolism. *Biotechnology and Bioengineering* **32**, 1053-1060.

Heidemann, S. R., Kaech, S., Buxbaum, R. E. and Matus, A. (1999). Direct observations of the mechanical behaviors of the cytoskeleton in living fibroblasts. *Journal of Cell Biology* **145**, 109-122.

Helmke, B. P., Goldman, R. D. and Davies, P. F. (2000). Rapid displacement of vimentin intermediate filaments in living endothelial cells exposed to flow. *Circulation Research* **86**, 745-752.

Helmke, B. P., Rosen, A. B. and Davies, P. F. (In press). Mapping mechanical strain of an endogenous cytoskeletal network in living endothelial cells. *Biophysical Journal*.

Helmke, B. P., Thakker, D. B., Goldman, R. D. and Davies, P. F. (2001). Spatiotemporal analysis of flow-induced intermediate filament displacement in living endothelial cells. *Biophysical Journal* **80**, 184-194.

Levitan, I., Helmke, B. P. and Davies, P. F. (2000). A chamber to permit invasive manipulation of adherent cells in laminar flow with minimal disturbance of the flow field. *Annals of Biomedical Engineering* **28**, 1184-93.

Wang, N., Butler, J. P. and Ingber, D. E. (1993). Mechanotransduction across the cell surface and through the cytoskeleton. *Science* **260**, 1124-1127.

FIGURE LEGENDS

Figure 1 Continuous closed flow loop for long-term live cell microscopy. Fluid flows by gravity from an upper reservoir through the flow chamber positioned on the microscope stage and into a lower reservoir. A peristaltic pump continuously recirculates the fluid from the lower reservoir back into the upper reservoir. A gas mixture of 5% CO2-95% air bubbled through sterile water in an adjacent humidifying chamber maintains pH in bicarbonate-buffered fluid. Both the lower reservoir and humidifying chamber are placed in a water bath warmed to 37 ºC <degrees C> to maintain temperature (not shown).

Figure 2 (A) Components and (B) side view of the MIF device that permits physical access to cells through slits in the top of a parallel plate flow chamber. (C) The MIF device mounted on a microscope stage with a typical electrophysiological micropipette lowered into the recording chamber. Adapted from (Levitan et al., 2000) with permission.

Figure 3 Examples of MIF chamber uses include (A) membrane aspiration and (B) cell prodding, (C) microinjection, (D) local release of solutes, and (E) biosensing of locally released cell products. From (Levitan et al., 2000) with permission.

Figure 4 (A) Optical section GFP-vimentin intermediate filament network near the apex of living endothelial cells within a confluent monolayer. Scale bar, 10 μm <micrometer>. (B) Magnified view of inset indicated in (A). Scale bar, 2 μm <micrometer>. (C) Small random displacement of GFP-vimentin illustrated by comparing false-colored images at the beginning (red) and end (green) of a 3-min interval with no flow. Yellow indicates zero displacement. (D) Significant displacement of intermediate filaments shown by colored images at the beginning (red) and end (green) of a 3-min interval just after onset of shear stress (13 dyn/cm^2, left to right). Adapted from (Helmke et al., 2000) with permission.

Figure 5 (A) Comparison of skeletons extracted from an optical section of GFP-vimentin just before (red) and 3 min after (green) onset of shear stress (12 dyn/cm^2, left to right). (B) Vertex displacement field from the inset box in (A) indicated by arrows on the skeleton. (C) Delaunay triangulation of vertices in the optical section in (A) to connect adjacent vertices on the skeleton for interpolation of the strain field. (D) Magnitude of principal stretch ratio λ_1 <lambda> indicating distribution of maximum strain during the 3-min interval after onset of shear stress. Note strain focusing corresponds to locations of dense interconnections among intermediate filament segments on the skeleton in (A). Adapted from (Helmke et al., In press) with permission.

Movie 1 Time lapse movie of deconvolved optical section demonstrating intracellular GFP-vimentin filament movement in 90-second intervals (green) superimposed on stationary images (red) selected at the start of the no-flow and flow periods. Separation of green and red indicates intermediate filament movement; yellow

represents zero displacement compared to the beginning of the period. Flow direction, left to right; shear stress, 12 dyn/cm^2; scale bar, 2 μm <micrometer>. Elapsed time, mm:ss. From (Helmke et al., 2000) with permission. Macintosh QuickTime™ (.mov) and Windows MPEG (.mpg) video formats are included.

Movie 2 Time-lapse movie of deconvolved optical section showing GFP-vimentin filament movement near the apical cell surface, corresponding to the region shown in Figure 4 B-D. Intermediate filament motion in 90-second intervals (green) is superimposed on stationary images (red) selected at the start of the no-flow and flow periods. Separation of green and red indicates intermediate filament movement; yellow represents Separation of green and red indicates intermediate filament movement; yellow represents zero displacement compared to the beginning of the period. Flow direction, left to right; shear stress, 12 dyn/cm^2; scale bar, 2 μm <micrometer>. Elapsed time, mm:ss. From (Helmke et al., 2000) with permission. Macintosh QuickTime™ (.mov) and Windows MPEG (.mpg) video formats are included.

FLOW LOOP

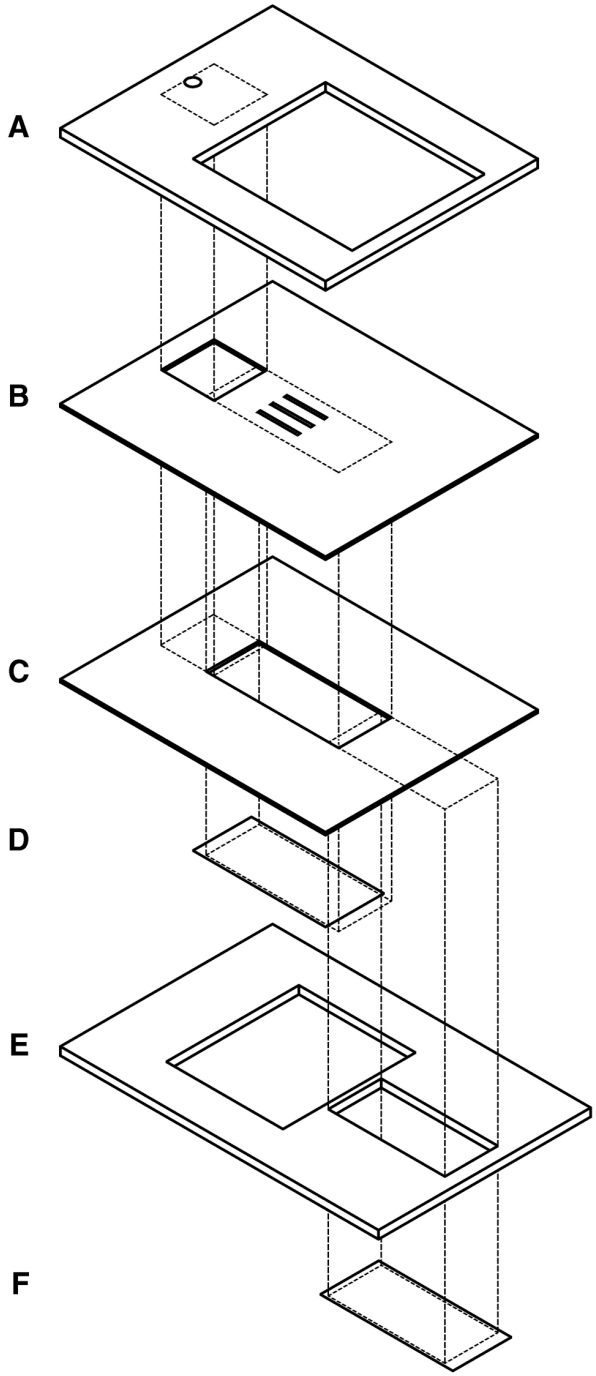

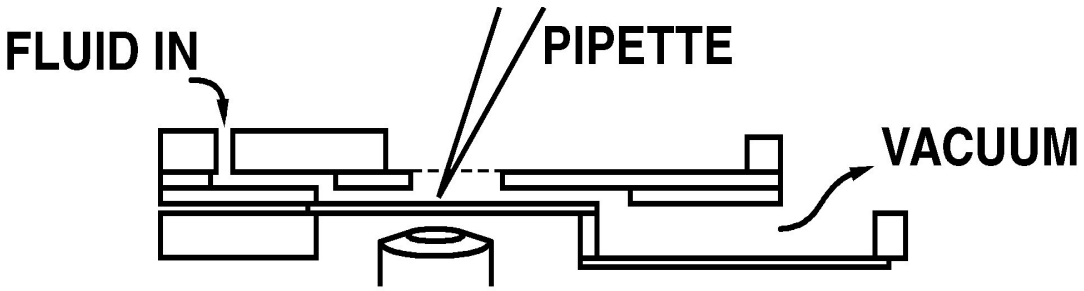

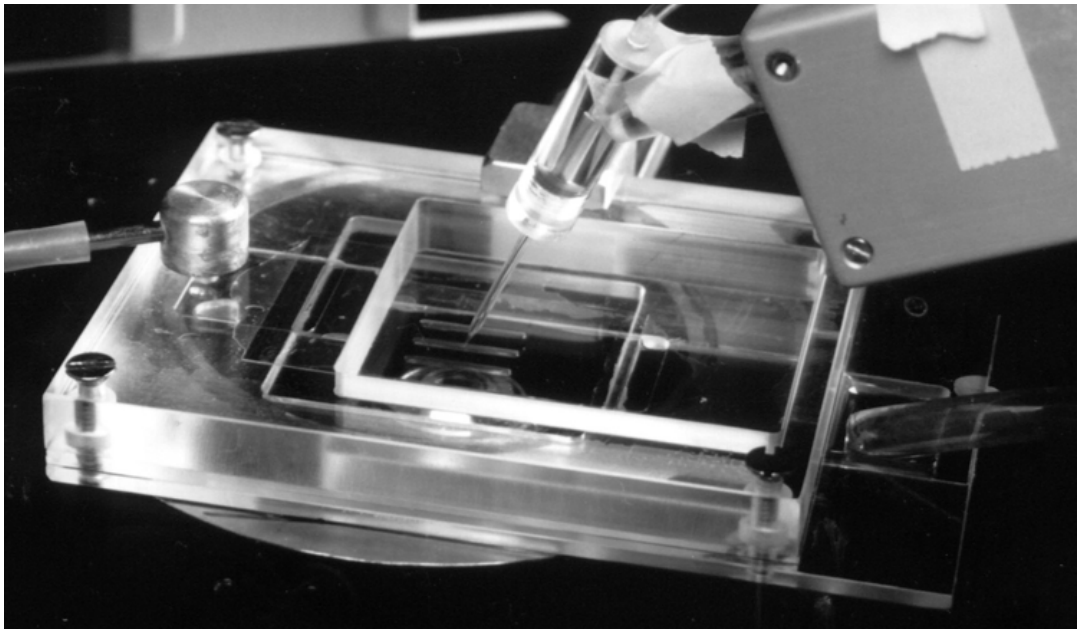

Figure 2

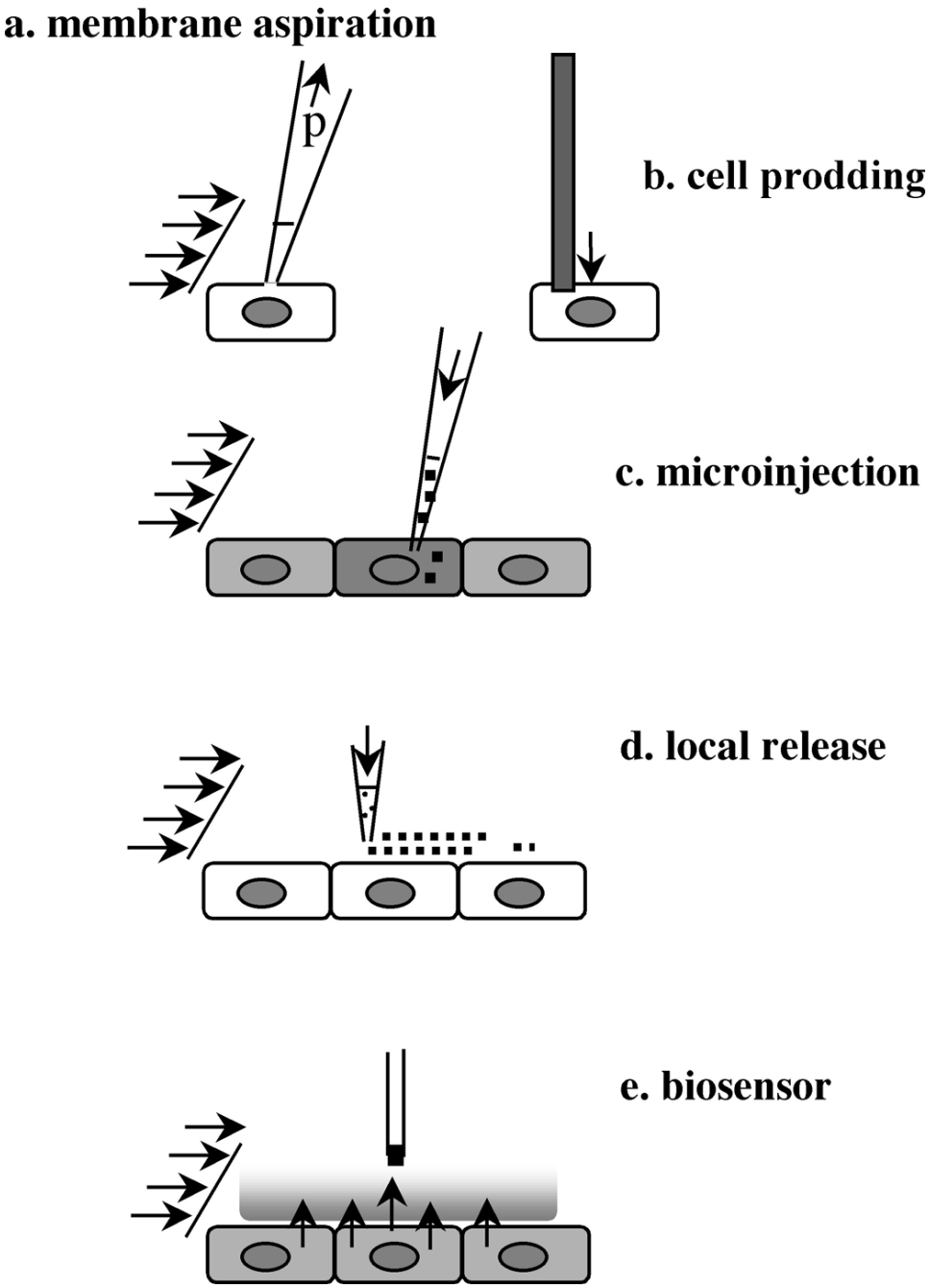
a. membrane aspiration
p
b. cell prodding
c. microinjection
d. local release
e. biosensor

Figure 3

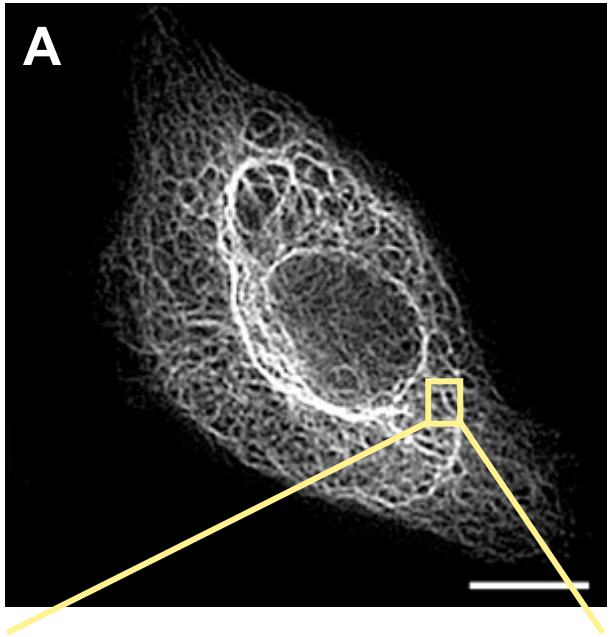

QuickTime™ and a
None decompressor
are needed to see this picture.

0 - 180 sec

NO FLOW

QuickTime™ and a
None decompressor
are needed to see this picture.

QuickTime™ and a
None decompressor
are needed to see this picture.

FLOW
(13 dyn/cm^2)

Start

0 - 180 sec

Figure 4

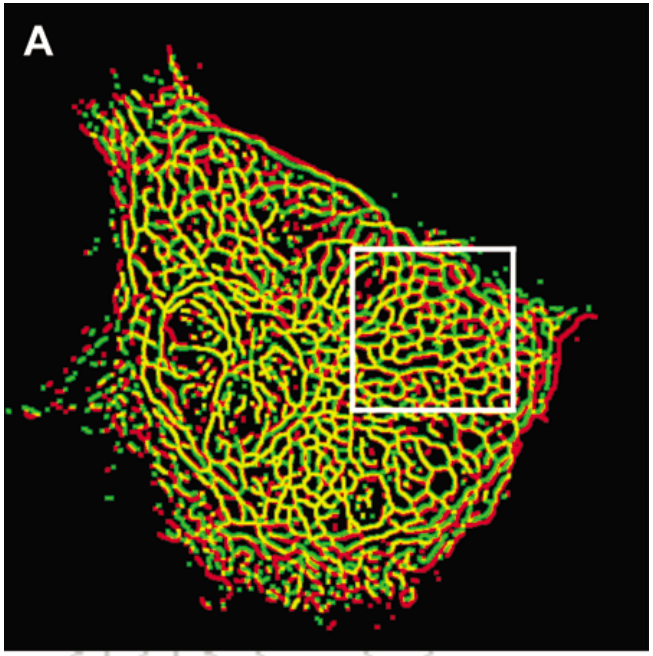

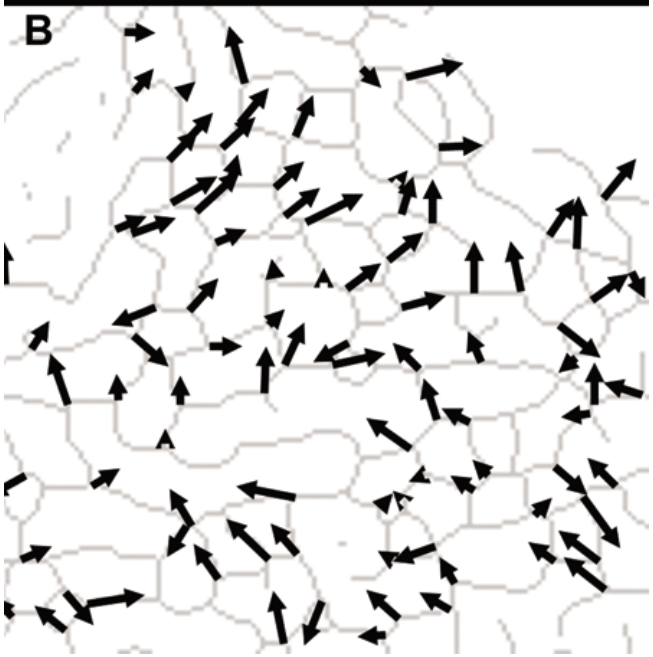

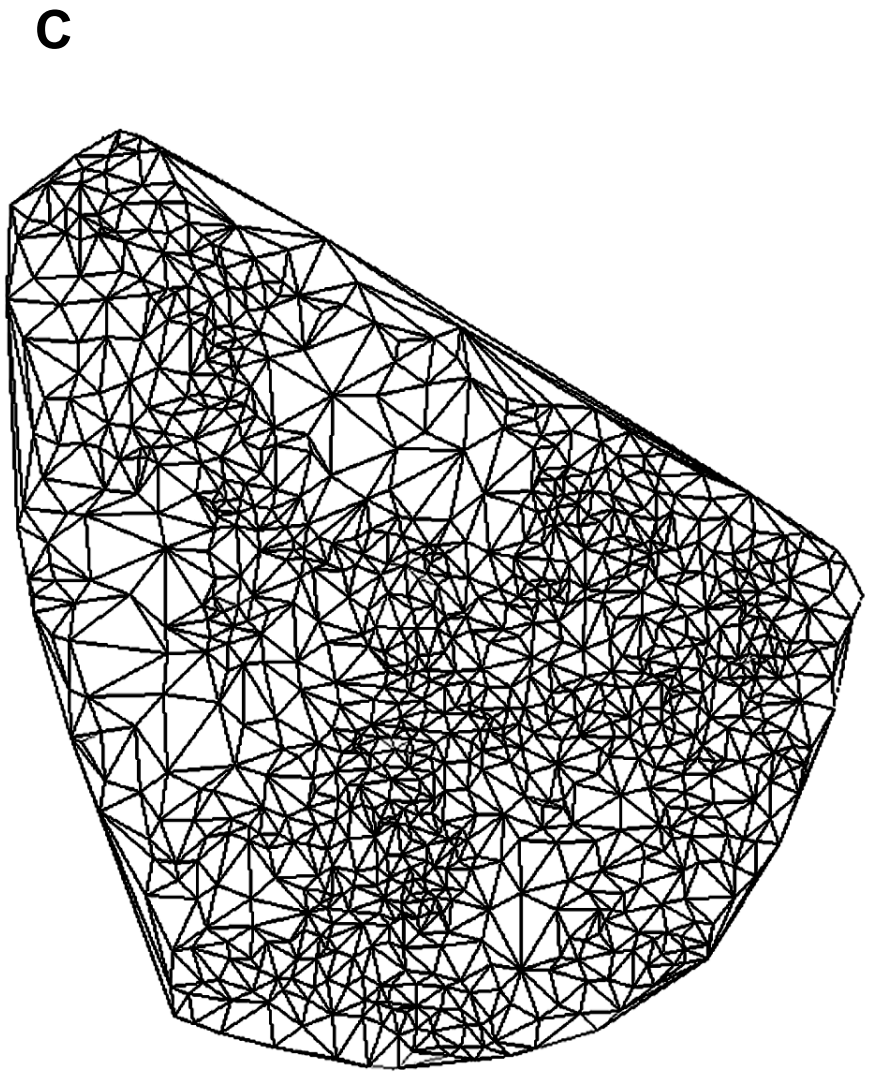

Figure 5

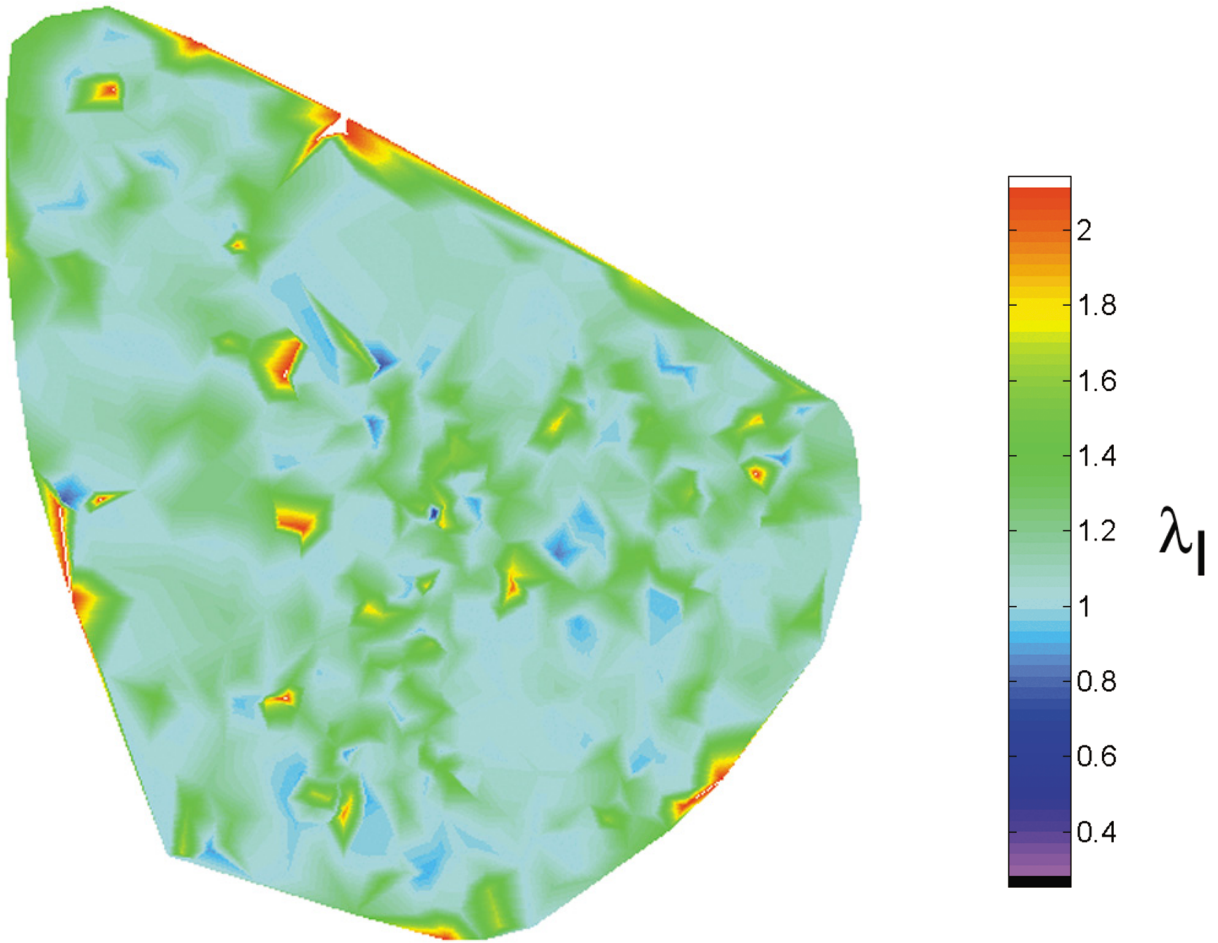

Figure 6